Thickness-Dependent Microstructure in Additively Manufactured Stainless Steel

Alexandra L. Vyatskikh, Thomas B. Slagle, Sen Jiang, Salma A. El-Azab, Umberto Scipioni Bertoli, Lorenzo Valdevit, Enrique J. Lavernia, and Julie M. Schoenung

Widespread industrial adoption of metal additive manufacturing (AM) requires an in-depth understanding of microstructural evolution during AM. In this study, the effect of process parameters and feature thickness on the microstructures of 316L stainless steel components fabricated by laser powder bed fusion (LPBF) was examined. A standard benchmark geometry developed by the National Institute of Standards and Technology, which contained walls of 0.5, 2.5 and 5.0 mm in thickness, was used. Optical microscopy, finite element analysis, scanning electron microscopy and electron backscatter diffraction revealed dramatic microstructural differences in features of different thickness within the same component. The feature thickness influenced the cooling rate, which in turn impacted the melt pool size, solidification microstructure, grain morphology and density of geometrically necessary dislocations. The relationship between feature size and grain morphology was dependent on the energy input used during LPBF. Such behavior suggested that local manipulation of LPBF process parameters can be employed to achieve microstructural homogeneity within the as-printed stainless steel components.

1. Introduction

Metal additive manufacturing (AM), also referred to as metal 3D printing, is poised to revolutionize the manufacturing industry by enabling shorter lead times, lightweighting through topology optimization, part count reduction and rapid production of parts with complex geometries (Ref 1). A remarkable recent example of successful AM implementation is the GE Aviation Catalyst turboprop engine, where AM enabled consolidation of 800 components into just 12 printed parts, reducing the engine's weight by 5% and improving its specific fuel consumption by 1% (Ref 2). Another notable example is NASA's 2020 Perseverance Mars rover, which features 11 3D printed parts (Ref 3). Use of AM in Perseverance's Planetary Instrument for X-ray Lithochemistry (PIXL) allowed for a three- to fourfold mass reduction in comparison with traditionally manufactured components. SpaceX's SuperDraco rocket engine powering the Crew Dragon manned spacecraft employs

Alexandra L. Vyatskikh, Thomas B. Slagle, Sen Jiang, Salma A. El-Azab, Umberto Scipioni Bertoli, Lorenzo Valdevit, Enrique J. Lavernia, and **Julie M. Schoenung**, Department of Materials Science and Engineering, University of California Irvine, 544 Engineering Tower, Irvine, CA 92617. Contact e-mail: julie.schoenung@uci.edu.

an additively manufactured Inconel thrust chamber (Ref 4). According to the company, use of metal AM in place of traditional machining resulted in an order of magnitude reduction in lead time, with the path from the initial concept to the first hotfire test taking just over three months (Ref 5).

These examples demonstrate that metal AM can be successfully implemented in critical aerospace components subjected to extreme environments. However, continued progress toward widespread industrial adoption of metal AM requires a comprehensive understanding of the local variations in phase composition, microstructure and mechanical properties caused by location-dependent thermal history of the parts. Such an understanding is especially important for geometrically complex components that contain features of different sizes, e.g., parts with integrated fluid/gas channels (Ref 6, 7). The relationship between feature size, microstructure and mechanical performance has been explored recently in 316L (Ref 8) and 304L (Ref 9) stainless steel parts fabricated by laser powder bed fusion (LPBF), Ti-6Al-4V parts produced by electron beam melting (EBM) (Ref 9-11), as well as LPBF-fabricated AlSi10Mg (Ref 12) and Inconel 625 (Ref 13). Roach et al. investigated microstructure and mechanical properties of 316L stainless steel parts of varying cross-sectional areas fabricated via LBPF (Ref 8). No clear relationship between the sample cross-sectional area and grain size, grain aspect ratio, sample crystallographic texture and microhardness was established. However, samples with larger cross-sectional areas tended to exhibit higher yield strength (YS), ultimate tensile strength (UTS) and elastic modulus, which was attributed to surface roughness effects. Brown et al. observed a similar trend in LPBF-fabricated 316L stainless steel and EBM-fabricated Ti-6Al-4V, where an increase in sample thickness induced an increase in YS and UTS in both materials—an effect that was also attributed to surface roughness and defects. However, a clear relationship between feature thickness, microstructure, phase composition and mechanical properties has not been established to date.

This work presents a step toward establishing a relationship between thickness and microstructural properties in stainless steel parts fabricated via laser powder bed fusion (LPBF). A standard, widely employed metal AM benchmark geometry developed by the National Institute of Standards and Technology (NIST) (Ref 13-16) was used. The benchmark components were fabricated from 316L stainless steel, a very low-carbon austenitic stainless steel which is a popular metal AM material (Ref 17-20) due to its ductility, high corrosion resistance and low propensity for chromium-rich carbide formation (Ref 21-23). Through a combination of 3D scanning, optical microscopy, finite element analysis (FEA), scanning electron microscopy (SEM) and electron backscatter diffraction (EBSD), dramatic microstructural variations within features of different thickness within the same component were observed. Overall, this work demonstrates that microstructural homogeneity within the as-printed stainless steel components that possess features of varying thickness can be achieved through local manipulation of LPBF process parameters.

2. Materials and Methods

2.1 Sample Fabrication

For this study, the AMB2018-01 bridge structure geometry developed by NIST (Fig. 1a) was used. The benchmark part is 75 mm long, 12 mm tall and 5 mm wide, with 12 "legs" of three different thicknesses: four 5.0-mm legs, four 2.5-mm legs and four 0.5-mm legs. The samples were fabricated using a commercial SLM 125HL LPBF system (SLM Solutions, Lübeck, Germany). The chamber was kept in an inert nitrogen atmosphere, with oxygen level maintained at <100 ppm. Two samples were printed concurrently on the same annealed 316L stainless steel build plate. The build plate was preheated to and maintained at 200 °C. Gas atomized 316L stainless steel powder (SLM Solutions, Lübeck, Germany) with $d_{10} = \sim 25$ μm, $d_{50} = \sim 40$ μm and $d_{90} = \sim 61$ μm was used as feedstock powder. Manufacturer-specified chemical composition of the powder is provided in Table 1. Laser spot size was set to 80 μm. Samples were denoted as B120 and B200, with the number reflecting the approximate volumetric energy density (VED, J/mm^3) used during fabrication. VED, E_v, is defined as (Ref 24):

$$E_v = \frac{P}{v \cdot t \cdot h} \tag{Eq 1}$$

where P is the laser power (W), v is the laser scan speed (mm/s), t is the layer thickness (mm) and h is the hatch spacing (mm). The LPBF process parameters shown in Table 2 were selected on the basis of fabricating as-printed parts with > 99% density.

2.2 Characterization

The bridge structures were separated from the substrate using wire electrical discharge machining (wire-EDM). After separation from the substrate, the samples were imaged using an ATOS Core 200 3D scanner (GOM, Braunschweig, Germany). The 3D scans were processed with CloudCompare open source point cloud processing software, where the 3D scans were overlayed with the nominal CAD geometry, and cloud-to-mesh (C2M) distances were computed.

Legs of 0.5, 2.5 and 5.0 mm in thickness were then separated from the bridge structure using wire-EDM (Fig. 1b). For examination under an optical microscope (OM) and scanning electron microscope (SEM), the legs were hot-mounted in Konductomet conductive filled phenolic mounting compound (Buehler, Lake Bluff, IL, USA) with the y-z surface exposed. Metallographic grinding was performed with 120-1200 grit silicon carbide papers using an AutoMet 250 grinder/polisher (Buehler, Lake Bluff, IL, USA). The samples were then polished with 3 and 1 μm DiaLube diamond suspensions on White Label woven silk polishing cloth (Allied High Tech
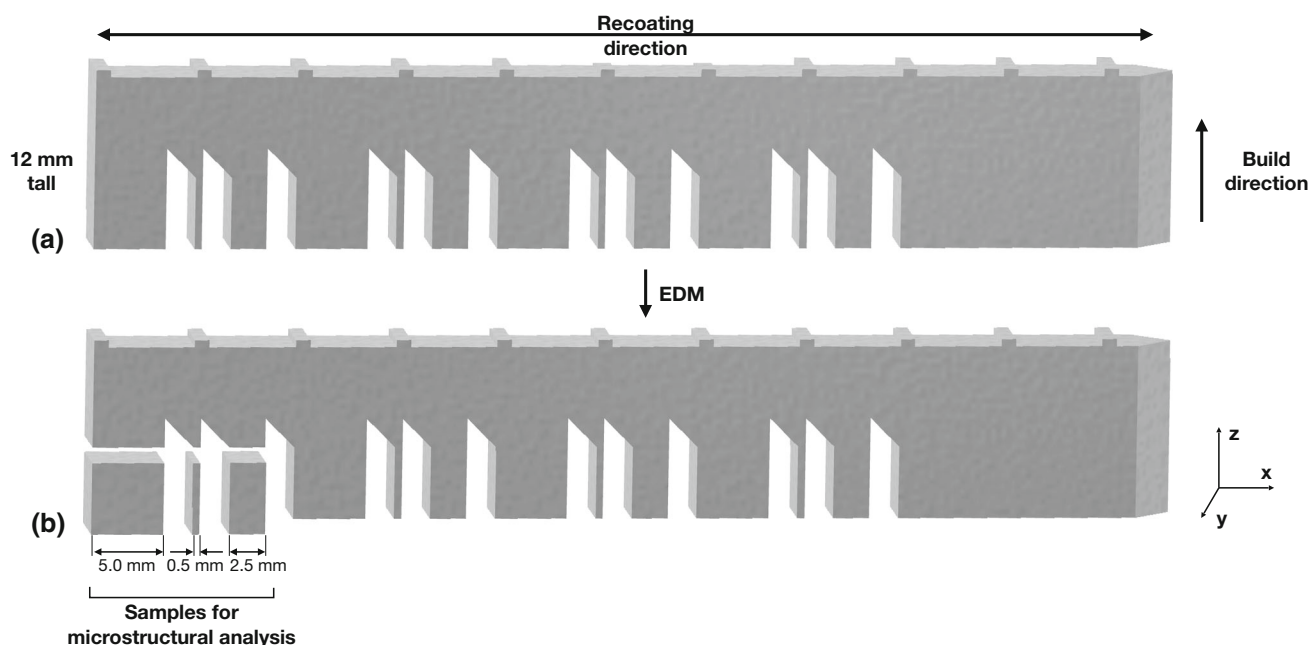
Fig. 1 The AMB2018-01 sample geometry used in the study. (a) 3D model of the AMB2018-01 bridge structure benchmark geometry. (b) Three legs (lower left corner) were separated from the parts for microstructural analysis using wire electrical discharge machining (wire-EDM)

Table 1. Chemical composition (mass fraction in %) of the feedstock powder, as provided by the manufacturer

Fe	Cr	Ni	Mo	Nb + Ta	Mn	Si	P	S	C	N	O
Balance	16.00-18.00	10.00-14.00	2.00-3.00	...	2.00	1.00	0.045	0.030	0.030	0.10	...

Table 2. Laser powder bed fusion (LPBF) process parameters used for sample fabrication. The calculated value for volumetric energy density is also provided

Sample ID	Laser power, W	Scan speed, mm/s	Hatch spacing, mm	Layer thickness, mm	Volumetric energy density, J/mm³
B120	195	800	0.10	0.02	122
B200	370	2520	0.04	0.02	196

Products, Inc., Rancho Dominguez, CA, USA). A final precision polish was obtained from vibratory polishing (GIGA-0900, PACE Technologies, Tucson, AZ, USA) for ~5 h using a 0.05 μm alumina suspension (PACE Technologies, Tucson, AZ, USA) mixed with deionized water. To reveal the solidification microstructures, the samples were etched using a 3:1 volume mixture of HCl and HNO_3 for 30 s. Immediately following the immersion in the acid solution, the samples were placed in a cold water bath to prevent overetching. Melt pool boundaries were identified from optical micrographs of the etched cross sections, and the melt pool widths and depths were measured using the ImageJ software (NIH) (Ref 25).

Electron backscatter diffraction (EBSD) mapping and forescattered electron (FSE) imaging were performed using a GAIA3 SEM-FIB dual-beam microscope (Tescan, Brno, Czech Republic) equipped with a NordlysMax2 detector (Oxford Instruments, Abingdon, Oxfordshire, UK). The microscope was operated in field mode at an accelerating voltage of 20 kV, beam intensity of 20 and working distance of ~ 5 mm. Samples were mounted on a 70° pre-tilted specimen holder. Two scans with 4x4 CCD camera binning were performed for each sample: (1) 1×1 mm map with a step size of 2 μm, and (2) 390×765 μm map with a step size of 1 μm. To avoid near-surface zones where grain refinement is possible, EBSD maps were collected from the middle regions of the specimen cross-sections.

EBSD maps were post-processed using the open source MTEX Matlab toolbox (Ref 26). First, data points with mean angular deviation (MAD) of > 1° were removed. Then, grains were defined as areas of the map completely surrounded by boundaries with a misorientation > 5°, and grain reconstruction was performed. The orientation data were denoised and missing data were interpolated using the half-quadratic filter (Ref 27). Grain aspect ratio was calculated as the ratio of the long axis length to the short axis length of the ellipses fitted to the grains. Kernel average misorientation (KAM) was computed using the first-order neighbors. Density of geometrically necessary dislocations (GNDs) was calculated following the approach suggested by Pantleon (Ref 28) based on local orientation changes.

SEM imaging for primary dendrite arm spacing (PDAS) measurements was performed using the Magellan 400 XHR microscope (FEI, Hillsboro, OR, USA). PDAS was calculated based on a series of SEM micrographs using the modified Abrams three-circle procedure as described in ASTM E112

(Ref 29). After the PDAS values were obtained, the corresponding cooling rates were calculated as (Ref 30):

$$d_p = 80(CR)^{-0.33} \qquad (Eq\ 2)$$

where d_p is the PDAS (μm) and CR is the corresponding cooling rate (°K/s).

Powder x-ray diffraction (XRD) patterns were collected with a diffractometer equipped with a 2.2 kW Cu-Ka x-ray source (Smartlab, Rigaku, Tokyo, Japan) configured in Bragg-Brentano geometry. The patterns were collected in the 2θ range of 20-120° with 0.02° step and at a scan speed of 4°/s.

2.3 Finite Element Analysis (FEA) Heat Flow Modeling

To simulate heat transfer during LPBF, a 3D FEA model was constructed in COMSOL 5.3a Multiphysics® software. Three geometries were meshed, corresponding to the 0.5, 2.5 and 5 mm legs (Fig. 2). The finer meshed regions were assigned to the features scanned by the laser beam. The coarser meshed regions represented the powder bed surrounding the deposited build and were assumed to have a thermal conductivity of 0.01 times of the bulk SS 316L alloy (Ref 31). Rectangular elements with a maximum size of 0.03 mm were used for the central, finer meshed region, and free tetrahedral elements with a maximum size of 0.28 mm were used for the coarser meshed regions. To simulate the laser deposition process, the thermal conductivity of the elements switched from that of the loose powder to that of solid bulk SS 316L after the laser spot moved past the elements. The simulations were performed for the entire 100th layer (2 mm away from the substrate) using both parameter sets described in Table 2. The laser spot was assumed to be a circular heat source 80 μm in diameter with uniformly distributed energy density. The laser spot followed a serpentine scan path for the entire layer. Due to negligible contributions of convective and radiative mechanisms to the heat transfer, only heat conduction was considered in this simulation, for which the governing equation is:

$$Q = \rho \cdot C_p \cdot \frac{\partial T}{\partial t} + \rho \cdot C_p \cdot v \cdot \nabla T - \nabla(k \cdot \nabla T) \qquad (Eq\ 3)$$

where Q is heat generated by laser beam (w/m²); ρ, C_p, k are the density (kg/m³), specific heat (J/(kg K)) and thermal conductivity (W/(m K)) of SS 316L, respectively; v is laser scan speed (m/s). The values for ρ, C_p, k were adopted from (Ref 32).

3. Results

First, the bulk geometry of the as-printed bridge samples was evaluated. The total length and width as measured from the 3D scans were 76.08 × 5.25 mm and 76.20 × 5.55 mm for samples B120 and B200, respectively. The C2M distances are plotted in Fig. 3(a) and (b), and the corresponding C2M histograms are shown in Fig. 3(c). The median C2M distance was ~ 53 μm for sample B120 and ~ 167 μm for sample B200. While both samples were found to be larger than the original CAD geometry (75 mm long and 5 mm wide), the deviation from the input file was greater for sample B200, which was fabricated with a higher energy input. A 61% increase in VED correlated with a ~ 215% increase in the median C2M distance. It is therefore evident that the dimensional accuracy of the as-printed parts was significantly affected by the process parameters used during LPBF processing. Deviation of part geometry from the input CAD file should be taken into consideration in further benchmark investigations.

Next, the melt pool geometries of the as-printed samples were analyzed. For sample B120, no clear trend could be identified in melt pool depth as a function of leg thickness, with measured mean pool depth of 29.2 ± 1.0, 27.9 ± 1.4 and 28.8 ± 1.14 μm for the 0.5, 2.5 and 5.0 mm thick legs, respectively (Fig. 4a). For sample B200, however, the mean melt pool depth decreased with increasing leg thickness, from 22.8 ± 1.8 to

21.6 ± 1.7 and to 14.2 ± 1.2 μm for the 0.5, 2.5 and 5.0 mm thick legs, respectively. For both samples B120 and B200, the melt pool width decreased with increasing leg thickness (Fig. 4b). For sample B120, the measured mean melt pool widths were 121.1 ± 3.4, 105.3 ± 3.4 and 105.6 ± 2.4 μm for the 0.5, 2.5 and 5.0 mm thick legs, respectively. For sample B200, the melt pool widths were 112.4 ± 7.8, 98.6 ± 7.4 and 94.1 ± 5.5 μm for the 0.5, 2.5 and 5.0 mm thick legs, respectively. Overall, melt pool was both shallower and narrower for sample B200.

FEA modeling confirmed that melt pool dimensions should, in general, be smaller in sample B200 than in sample B120. The FEA model tended to overestimate the melt pool dimensions for both samples while capturing the trends observed in the experimental data (Fig. 4a, b). Overestimation of the melt pool dimensions by the FEA model can be potentially attributed to the simplification that ignores the Marangoni convective fluid flow in the melt pool (Ref 24). Smaller depth and width of the melt pool in sample B200 can be attributed to a more elongated, teardrop-like shape of the melt pool along the scanning direction, as illustrated by the temperature profiles extracted from the FEA model (Fig. 4c, d).

Further microstructural characterization was performed via a quantitative analysis of the grain structure of the samples. For sample B120, inverse pole figure (IPF) maps overlayed over
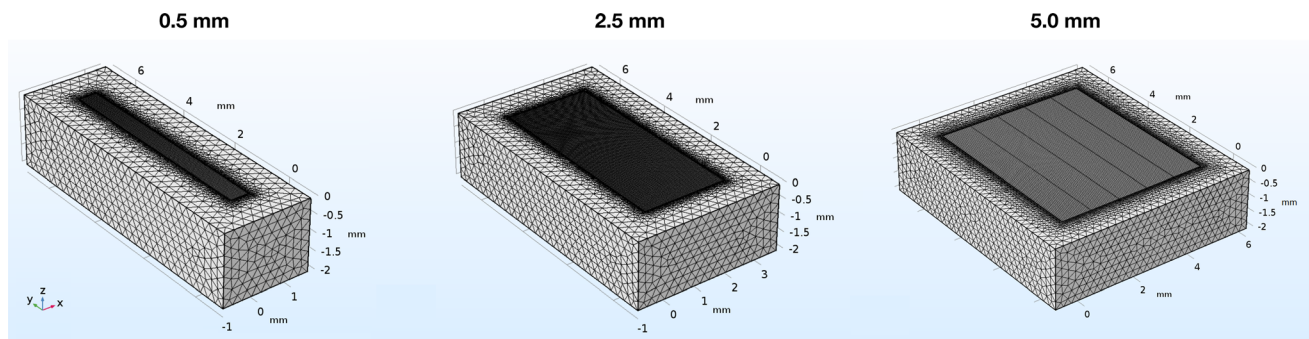

Fig. 2 Meshed geometries for finite element analysis (FEA) of heat flow within features of different thicknesses
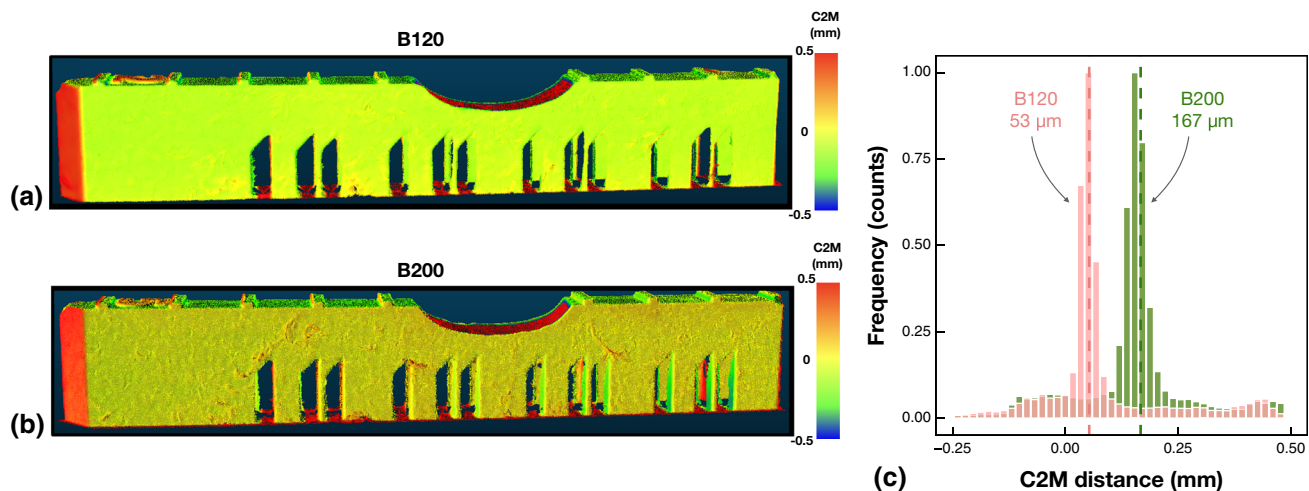
Fig. 3 Dimensional accuracy of the as-printed AMB2018-01 bridge structures. Cloud-to-mesh (C2M) distances plotted over the 3D scans of the (a) sample B120, and (b) sample B200. (c) Histogram plots of the C2M distances, with dashed vertical lines indicating median C2M distances
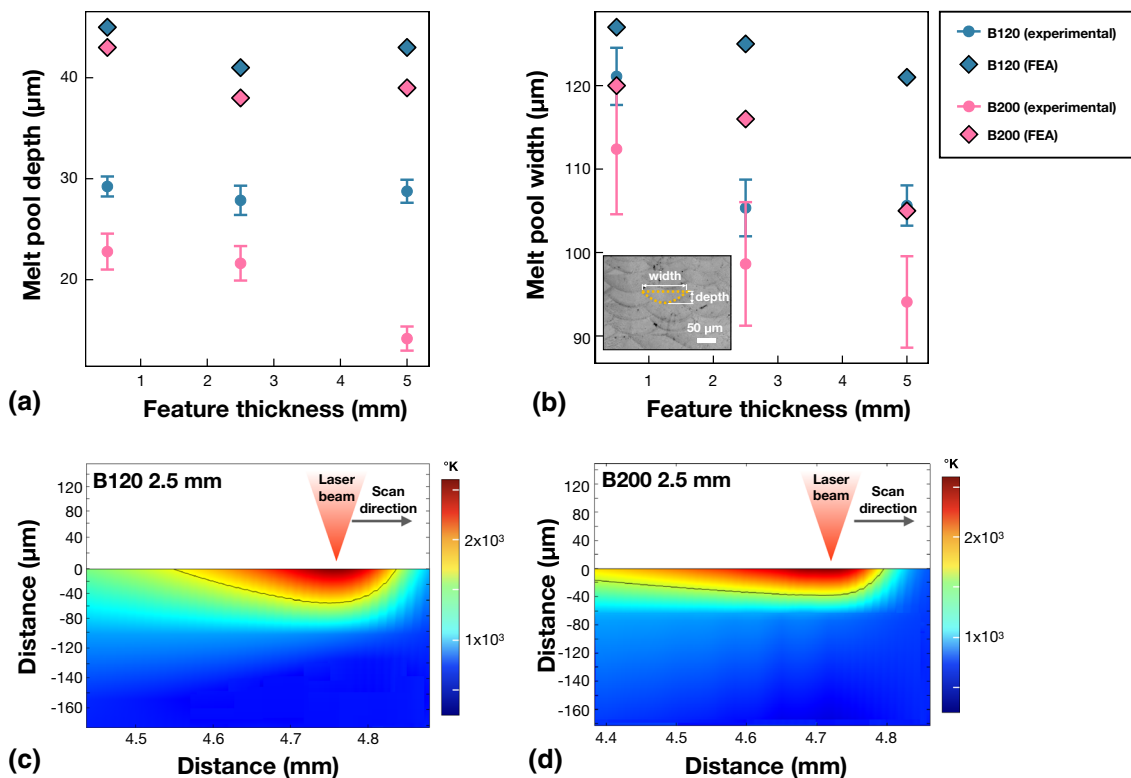
Fig. 4 Melt pool geometry within the as-printed AMB2018-01 bridge structures. Measured and simulated melt pool (a) depth, and (b) width as a function of feature thickness, with a representative optical micrograph of the etched microstructure showing melt pool fusion lines in the inset. Temperature profiles generated by the finite element analysis (FEA) model for (c) sample B120, and (d) sample B200 illustrate differences in melt pool geometries (solid black lines indicate liquidus isotherms for 316L stainless steel). Error bars represent 95% confidence intervals

FSE images are shown in Fig. 5a. Within the 0.5 mm thick leg, the grains had irregular, faceted morphologies. For the 2.5-mm thick leg, grains formed long columns of ~ 62 μm in width, with smaller grains located between the adjacent large columnar grains. A similar grain structure was observed for the 5.0 mm leg, where the width of the columnar grains was ~ 80 μm. Mean grain areas for sample B120 were 718 ± 102, 764 ± 188 and 912 ± 208 μm^2 for the 0.5, 2.5 and 5.0 mm thick legs, respectively. For sample B200, IPF maps overlayed over FSE micrographs are shown in Fig. 5b. Within the 0.5 mm thick leg, the grains were highly elongated and aligned along a direction rotated $\sim 30°$ with respect to the build direction. In the 2.5 and 5.0 mm thick legs, grains had irregular, faceted shapes and were aligned along the build direction. Mean grain areas for sample B200 were 1936 ± 483, 922 ± 181 and 546 ± 65 μm^2 for the 0.5, 2.5 and 5.0 mm thick legs, respectively.

Opposite trends in grain area as a function of feature thickness were identified in samples B120 and B200 (Fig. 5c): in B120, grain area increased with feature thickness (a $\sim27\%$ increase in grain area in the 5.0 mm thick leg as compared to that in the 0.5 mm leg), while in B200, grain area decreased with feature thickness (a $\sim 72\%$ decrease in grain area in the 5.0 mm thick leg as compared to that in the 0.5 mm thick leg). Similar trends were observed in grain aspect ratios (ARs) as a function of feature thickness (Fig. 5d): in sample B120, grains became more elongated as feature thickness increased (with ARs of 3.3 and 4.9 for the 0.5 and 5.0 mm thick legs, respectively), while in B200, grains tended to be more equiaxed in thicker features (AR of 4.9 and 3.4 for the 0.5 and 5.0 mm thick legs, respectively).

To understand the factors that influence microstructure evolution, the solidification microstructures and the corresponding cooling rates were assessed. A representative secondary electron (SE) micrograph of the solidification microstructure is shown in Fig. 6(a). Cooling rates calculated based on PDAS are plotted as a function of feature thickness in Fig. 6(b). No clear trend was identified in cooling rate as a function of feature thickness in sample B120, where cooling rates were calculated to be 11×10^5, 17×10^5 and 11×10^5 °K/s within the 0.5, 2.5 and 5.0 mm thick legs, respectively. For sample B200, the cooling rates were found to be 3×10^5, 6×10^5 and 6×10^5 °K/s within the 0.5, 2.5 and 5.0 mm thick legs, respectively, indicating a slight increase in cooling rate with increasing feature thickness. Overall, cooling rates were lower in sample B200 in comparison with sample B120, which is in agreement with previous experimental results (Ref 33) and numerical simulations (Ref 33, 34) of LPBF of 316L stainless steel.

The analysis was further extended with an investigation of the effect of feature thickness on the phase composition and microsegregation within the as-printed samples. XRD analysis of samples B120 (Fig. 7a) and B200 (Fig. 7b) revealed that the face-centered γ-austenite was the main phase present in the samples. Additionally, a diffraction peak indexed to the (110) set of lattice planes of the body-centered cubic δ-ferrite phase was observed at $\sim 43.5°$ for all three leg thicknesses of sample B120, and this peak was most prominent for the 0.5 mm thick leg. Oval-shaped δ-ferrite particles were observed in the SE micrographs of the 0.5 mm thick leg of sample B120 (Fig. 7c) at the austenite cell boundaries. In sample B200, no clear peaks
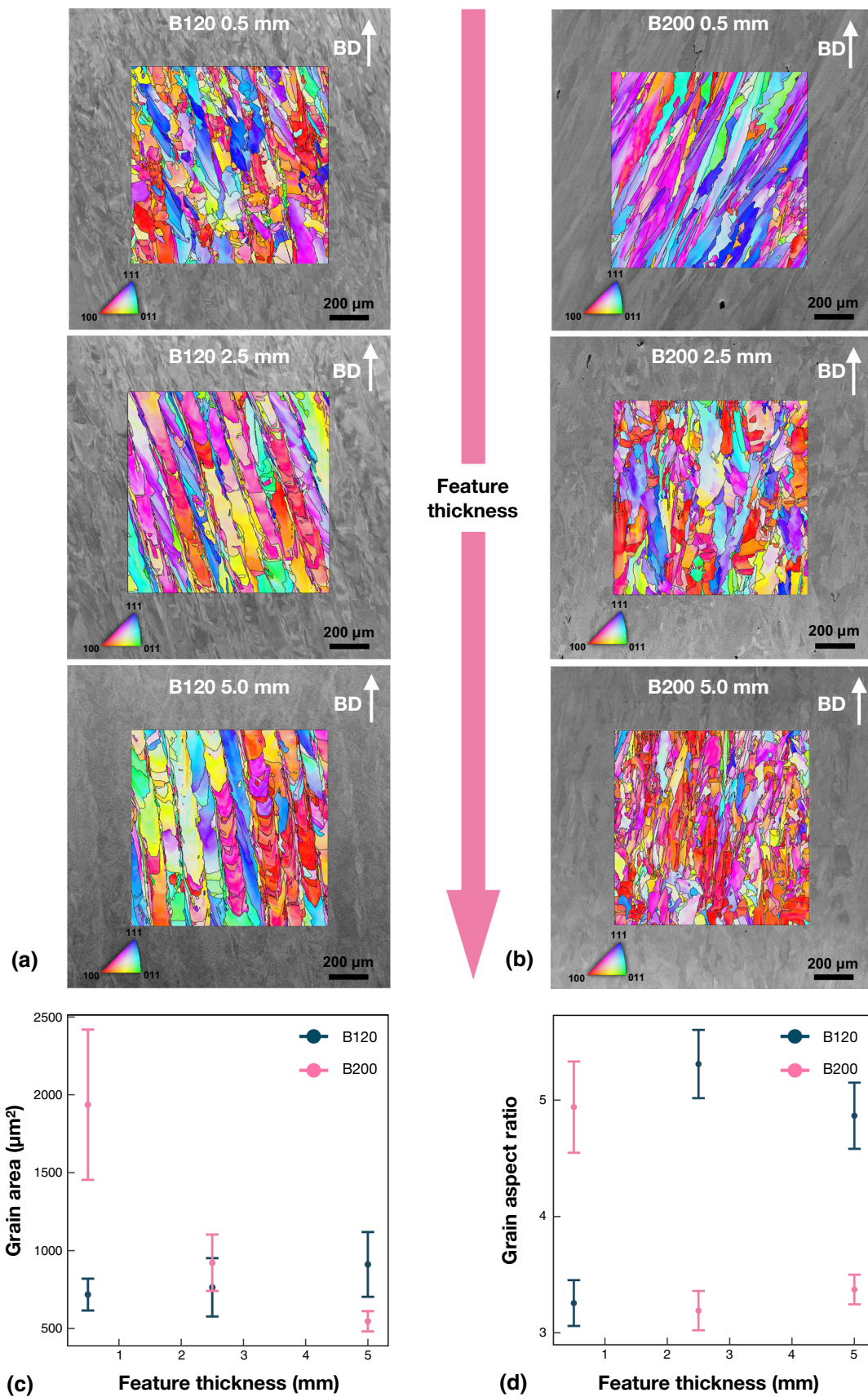
Fig. 5 Analysis of the grain structure. Inverse pole figure (IPF) maps overlayed over forescattered electron (FSE) images for (a) sample B120 and (b) sample B200; (c) grain area as a function of feature thickness; (d) grain aspect ratio as a function of feature thickness. Error bars represent 95% confidence intervals
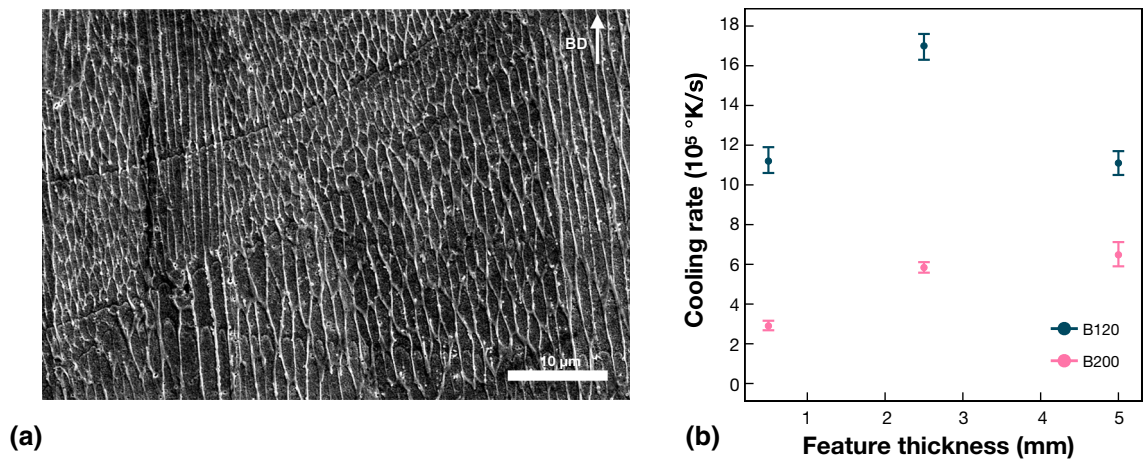
Fig. 6 Solidification microstructure and cooling rates in SS316L builds. (a) A representative secondary electron (SE) micrograph of the solidification microstructure. (b) Cooling rates calculated based on primary dendrite arm spacing (DAS). Error bars represent 95% confidence intervals
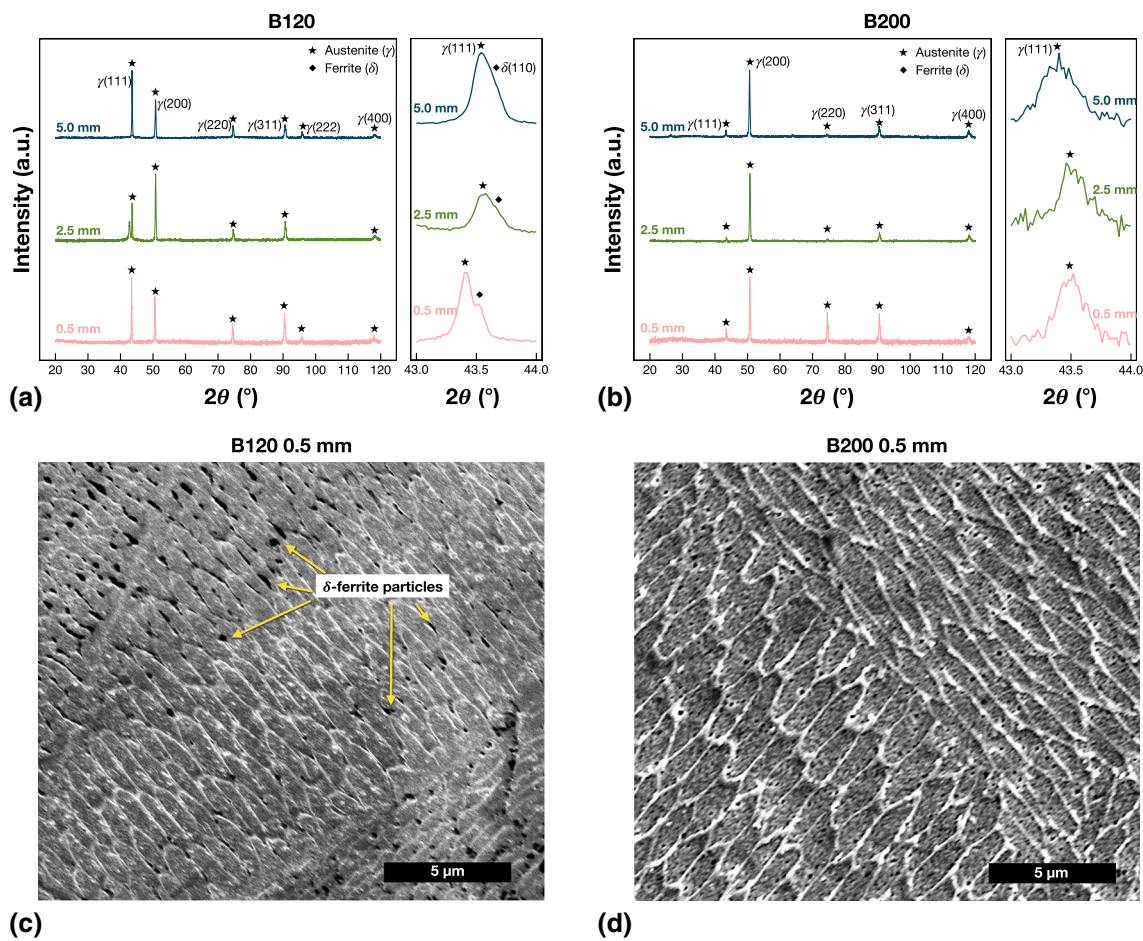

Fig. 7 Phase composition of the as-printed SS316L samples: (a) X-ray diffraction (XRD) patterns for sample B120, (b) XRD patterns for sample B200, (c) secondary electron (SE) micrograph of the microstructure for the 0.5 mm thick leg of sample B120, (d) SE micrograph of the microstructure for the 0.5 mm thick leg of sample B200

corresponding to the δ-ferrite phase were identified in the XRD patterns (Fig. 7b), and no δ-ferrite particles were observed in the SE micrographs (Fig. 7d).

Finally, the influence of LPBF process parameters and local part geometry on local plastic deformation within the as-printed parts was investigated. IPF EBSD maps and the corresponding KAM maps for sample B120 are shown in Fig. 8(a). The mean KAM values were 0.30°, 0.26° and 0.28° for the 0.5, 2.5 and 5.0 mm thick legs, respectively, indicating no trend in KAM as a function of leg thickness in sample B120. IPF maps and the
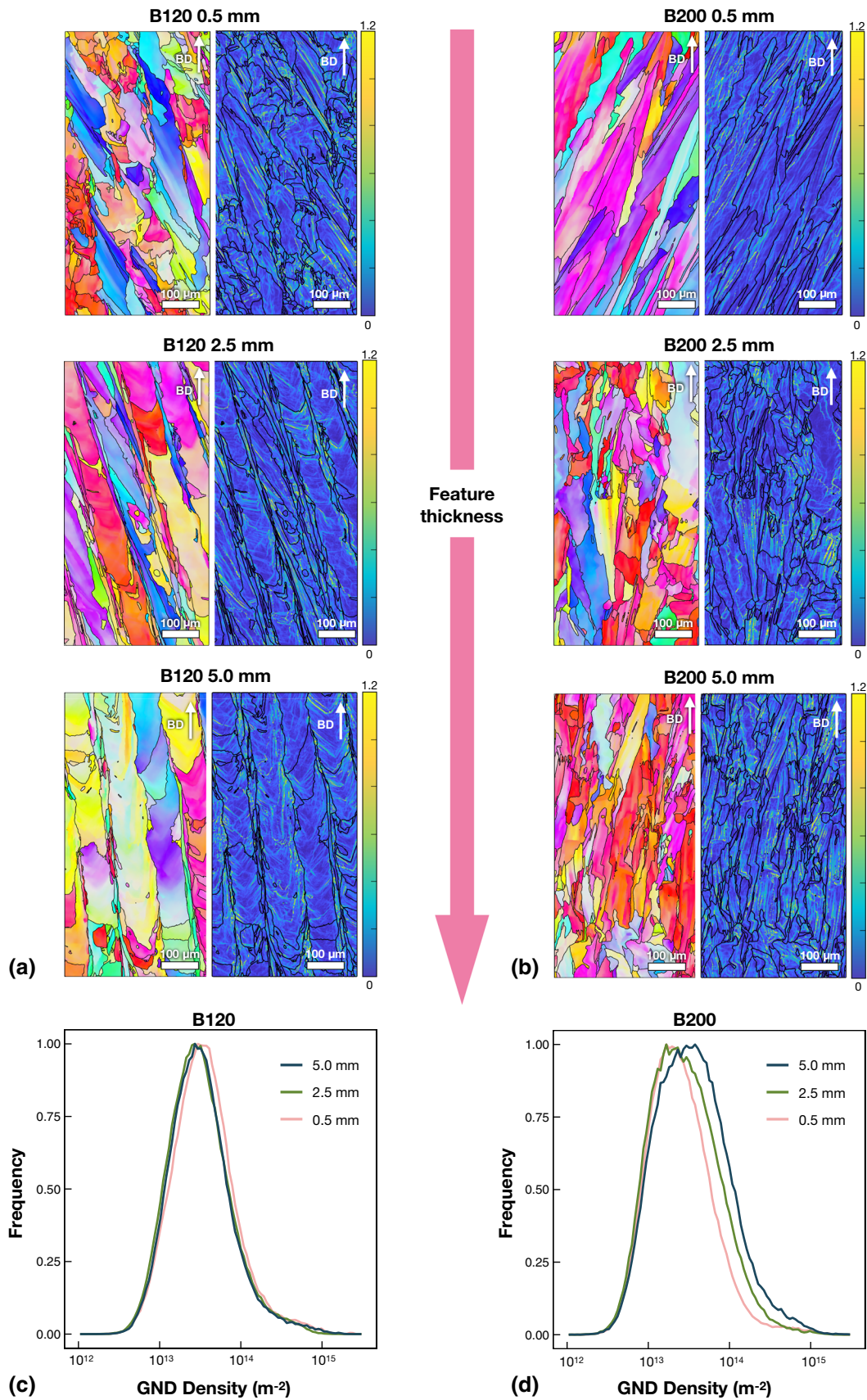
Fig. 8 Local plastic deformation within the as-printed samples. Inverse pole figure (IPF) maps and the corresponding kernel average misorientation (KAM) maps for (a) sample B120, and (b) sample B200. Distributions in the density of geometrically necessary dislocations (GNDs) for (c) sample B120, and (d) sample B200

corresponding KAM maps for sample B200 are shown in Fig. 8(b). The mean KAM values were 0.24°, 0.25° and 0.33° for the 0.5, 2.5 and 5.0 mm thick legs, respectively. In contrast to sample B120, a correlation between feature thickness and KAM was observed in sample B200, with thicker feature exhibiting higher KAM values.

Plots of the GND density distributions for sample B120 are shown in Fig. 8(c). Median GND density values were calculated to be 3.38×10^{13}, 2.93×10^{13} and 3.02×10^{13} m^{-2} for the 0.5, 2.5 and 5.0 mm thick legs, respectively. For sample B200, the GND density distributions are shown in Fig. 8(d), and median GND density values were calculated to be 2.29×10^{13}, 2.63×10^{13} and 3.33×10^{13} m^{-2} for the 0.5, 2.5 and 5.0 mm thick legs, respectively. Overall, the largest GND density of 3.33×10^{13} m^{-2} was observed in the 5.0 mm thick leg of sample B200.

4. Discussion

All key microstructural characteristics of the samples obtained from the SEM and EBSD analyses are summarized in Table 3. Both LPBF-printed benchmark parts investigated in this work exhibited cellular microstructures typical for additively manufactured 316L stainless steel (Fig. 7c and d) (Ref 35), with cell boundaries formed via microsegregation of Mo and Cr (Ref 20, 36, 37). For sample B120, the solidification mode was primary austenite with second-phase intercellular dendrite (Ref 38-41), with oval-shaped ferrite particles observed at the cell walls and triple points (Fig. 7c). Presence of δ-ferrite in sample B120 was additionally confirmed with XRD analysis (Fig. 7a), where the (110) peak of δ-ferrite was observed. In contrast to sample B120, retained δ-ferrite was not detected in sample B200 (Fig. 7b and d). Absence of XRD peaks attributed to δ-ferrite indicates that either there is no retained δ-ferrite present in sample B200 or it is present in amounts below the $\sim$ 3 vol.% detection limit of the laboratory XRD (Ref 42). Overall, the two-phase austenite-ferrite microstructure observed in sample B120 is not surprising. Based on the chemical composition of the feedstock powder (Table 1) and Schaeffler equivalency relationships (Ref 43), a nickel equivalent Ni_{eq} of 11.9-15.9 and a chromium equivalent Cr_{eq} of 19.5-22.5 can be expected for 316L stainless steel used in this work. Based on the Schaeffler diagram (Ref 43) and the values of Ni_{eq} and Cr_{eq}, the material is predicted to contain both austenite and ferrite, with the amount of δ-ferrite dependent on the alloy composition. A rough estimation of the amount of δ-

ferrite can be obtained from Seferian's relationship (Ref 44, 45), which yields $\sim$ 3.0-5.2 vol.% of δ-ferrite. Preferential formation of intercellular dendrite in sample B120 as compared to sample B200 can be attributed to the higher cooling rates observed in sample B120 (Fig. 6b), which potentially suppressed the ferrite to austenite transformation (Ref 46). Thus, the analysis of phase composition suggests that phase formation control via manipulation of LPBF process parameters is possible in 316L stainless steel and other materials that exhibit multiple phases.

Grain area and morphology were found to be a function of feature thickness for both samples. For sample B120, grain area increased from $\sim$ 718 μm^2 for the 0.5 mm leg to $\sim$ 912 μm^2 for the 5.0 mm leg (Fig. 8a), which constituted a $\sim$ 27% increase in grain area. An opposite trend was observed in sample B200, where grain area decreased $\sim$1936 μm^2 in the 0.5 mm leg to 546 μm^2 in the 5.0 mm leg (Fig. 8b), or a $\sim$ 72% decrease. The trend observed in sample B200 is in agreement with the calculated cooling rates (Fig. 5b), where an increase in cooling rate with increasing feature thickness was observed. However, cooling rates alone cannot explain the grain structure evolution observed in sample B120, suggesting that other factors (e.g., solidification rate (Ref 35) or temperature gradient (Ref 47)) have a dominant influence on grain growth in this sample.

Based on the Hall-Petch relationship (Ref 48, 49) and the observed grain sizes (Fig. 5c), a strong dependence of the mechanical properties on the feature size can be expected in sample B200. It can be speculated that in sample B200, strength should be proportional to the feature size, as larger features tended to exhibit smaller grain sizes. Similarly, some variation in strength can be expected in features of different thickness within sample B120, with thicker features exhibiting a slightly decreased strength.

Large, columnar grains spanning tens of layers were observed in the 2.5 and 5.0 mm thick legs of sample B120 (Fig. 5a) and in the 0.5 mm thick leg of sample B200 (Fig. 5b). Similar grain structures were previously reported for Inconel 625 parts printed for the AM Bench challenge (Ref 13), as well as LPBF-printed SS 316L (Ref 50, 51) and CrMnFeCoNi high-entropy alloy samples (Ref 50). Highly anisotropic grain structures observed in these samples can potentially cause significant anisotropy in mechanical properties (Ref 52) while also negatively affecting fatigue performance (Ref 53, 54) and corrosion resistance (Ref 55). Therefore, such anisotropic grain structures should be avoided.

Grain growth direction was influenced by the feature thickness. In sample B200, inclined grain orientations were

Table 3. Summary of key microstructural parameters depending on the feature size. Cooling rates, grain areas and grain aspect ratios are reported as mean values $\pm$ 95% confidence intervals

Sample ID	Feature thickness, mm	Cooling rate, 10^5 °K/s	Grain area, μm^2	Grain aspect ratio	Mean KAM[*], degrees	Median GND[*] density, 10^{13} m^{-2}
B120	0.5	11.20 ± 0.70	718 ± 102	3.26 ± 0.20	0.30	3.38
	2.5	17.00 ± 0.60	764 ± 188	5.31 ± 0.29	0.26	2.93
	5.0	11.10 ± 0.60	912 ± 208	4.87 ± 0.28	0.28	3.02
B200	0.5	2.90 ± 0.26	1936 ± 483	4.94 ± 0.39	0.24	2.29
	2.5	5.84 ± 0.27	922 ± 181	3.19 ± 0.17	0.25	2.63
	5.0	6.48 ± 0.64	546 ± 65	3.37 ± 0.13	0.33	3.33

KAM kernel average misorientation, *GND* geometrically necessary dislocations

observed in the 0.5 mm thick leg, while the 2.5 and 5.0 mm thick legs exhibited largely vertical grain orientations (Fig. 5b). The observed differences in grain growth directions in sample B200 can be attributed to differences in melt pool depth (Fig. 4a) (Ref 24). A deeper melt pool (~ 23 μm deep) observed in the 0.5 mm thick leg produced highly inclined grains, and a shallower melt pool (~ 14 μm deep) observed in the 5.0 mm thick leg generated grains oriented along the build direction.

Dislocation substructures and GND densities were found to depend on LPBF process parameters and feature thickness. In both samples, high-KAM regions were observed within the grains, indicating agglomeration of dislocations and formation of low-angle grain boundaries (Ref 56) (Fig. 8a and b). For sample B120, high-KAM lines were observed to form V-shaped channels (Fig. 8a, middle and right), while this behavior was not detected in sample B200 (Fig. 8b). GND densities were lognormally distributed within both samples (Fig. 8c and d) in agreement with previously published work (Ref 57). In sample B120, no clear relationship between feature thickness and GND density was identified (Fig. 8c), suggesting similar plastic deformation in features of all three thicknesses at the resolution afforded by EBSD mapping employed in this work. In contrast, in sample B200, GND density increased with feature thickness (Fig. 8d), indicating accommodation of higher thermal stresses through plastic deformation in features of larger thickness. To elaborate the evolution of strain and GND density in LPBF-printed parts, a further investigation via high-resolution EBSD (Ref 56) or precession electron diffraction (PED) is needed.

5. Conclusions

The influence of the local part geometry and LPBF process parameters on the microstructure of additively manufactured 316L stainless steel was explored. An extensive microstructural characterization of two LPBF-printed AMB2018-01 benchmark parts (sample B120, printed at a volumetric energy density (VED) of ~ 120 J/mm^3, and sample B200, printed at a VED of ~ 200 J/mm^3) was performed. The benchmark parts contained features of three thicknesses: 0.5, 2.5 and 5.0 mm. Specific findings are as follows:

1. Dimensional accuracy of LPBF-printed benchmark parts depended on the process parameters, with larger VED used during printing causing larger deviations from the input CAD geometry.
2. Evaluation of the melt pool geometry via optical microscopy coupled with a finite element analysis heat flow model showed that melt pool size varied with feature thickness. In sample B200, melt pool depth was inversely proportional to the feature thickness, while in sample B120, no direct relationship between feature thickness and melt pool depth was established. For both samples, melt pool width decreased with increasing feature thickness.
3. Melt pool depth, in turn, influenced grain growth direction within sample B200, where a shallower melt pool produced grains oriented along the build direction, and a deeper melt pool generated grains inclined with respect to the build direction.

4. No influence of feature thickness on phase composition was established. However, LPBF process parameters influenced the amount of retained δ-ferrite present within the samples: lower energy input used in sample B120 caused higher cooling rates and promoted suppression of the ferrite-austenite transformation; no δ-ferrite was observed in sample B200.
5. The relationship between grain morphology and feature thickness was highly dependent on the LPBF process parameters. In sample B120, an increase in feature thickness caused an increase in grain size, while an opposite trend was observed in sample B200.
6. Finally, density of geometrically necessary dislocations (GND)s was dependent on feature thickness in sample B200, where thicker features exhibited higher values of GND density, suggesting larger plastic deformation.

Overall, the present findings demonstrate that local part geometry has a significant influence on the solidification and grain microstructure of LPBF-printed parts. Microstructure within features of different thickness was found to be dependent on the LPBF process parameters (e.g., VED). Therefore, in complex parts, where both thick and thin features are present, microstructural homogeneity can be achieved by locally tailoring the LPBF process parameters, potentially eliminating the need for post-print heat treatment.

References

1. M. Orme, I. Madera, M. Gschweitl and M. Ferrari, Topology Optimization for Additive Manufacturing as an Enabler for Light Weight Flight Hardware, *Designs*, 2018, **2**, p 51
2. GE Additive, Why GE Additive's 3D Prtinted Catalyst Turboprop Engine Is Turning Heads? (2019). https://www.ge.com/additive/storie s/ge-additive-3d-printed-catalyst-turboprop-engine-turning-heads (accessed December 4, 2020)

3. A. Good, A. Johnson, G. Hautaluoma, NASA's Perseverance Rover Bringing 3D-Printed Metal Parts to Mars, (2020). https://www.nasa.gov/feature/jpl/nasas-perseverance-rover-bringing-3d-printed-metal-parts-to-mars (accessed December 4, 2020)

4. J.M. Waller, B.H. Parker, K.L. Hodges, E.R. Burke, J.L. Walker, Nondestructive Evaluation of Additive Manufacturing State-of-the-Discipline Report, 2014

5. C. Dordlofva, A. Lindwall, P. Törlind, Opportunities and challenges for additive manufacturing in space applications, in: Proc. Nord., 2016

6. F. Romei, A.N. Grubišić and D. Gibbon, Manufacturing of a High-Temperature Resistojet Heat Exchanger by Selective Laser Melting, *Acta Astronaut.*, 2017, **138**, p 356–368

7. C. Zhang, S. Wang, J. Li, Y. Zhu, T. Peng and H. Yang, Additive Manufacturing of Products with Functional Fluid Channels: A Review, *Addit. Manuf.*, 2020, **36**, p 101490

8. A.M. Roach, B.C. White, A. Garland, B.H. Jared, J.D. Carroll and B.L. Boyce, Size-Dependent Stochastic Tensile Properties in Additively Manufactured 316L Stainless Steel, *Addit. Manuf.*, 2020, **32**, p 101090

9. B. Brown, W. Everhart and J. Dinardo, Characterization of Bulk to Thin Wall Mechanical Response Transition in Powder Bed AM, *Rapid Prototyp. J.*, 2016, **22**, p 801

10. S.M.J. Razavi, B. Van Hooreweder and F. Berto, Effect of Build Thickness and Geometry on Quasi-Static and FATIGUE BEHAvior of Ti-6Al-4V Produced by Electron Beam Melting, *Addit. Manuf.*, 2020, **36**, p 101426

11. X. Tan, Y. Kok, Y.J. Tan, G. Vastola, Q.X. Pei, G. Zhang, Y.W. Zhang, S.B. Tor, K.F. Leong and C.K. Chua, An Experimental and Simulation Study on Build Thickness Dependent Microstructure for Electron Beam Melted Ti-6Al-4V, *J. Alloys Compd.*, 2015, **646**, p 303–309

12. A. Majeed, A. Ahmed, B. Liu, S. Ren and J. Yang, Influence of Wall Thickness on the Hardness of AlSi10Mg Alloy Parts Manufactured by Selective Laser Melting, *Procedia CIRP.*, 2019, **81**, p 459–463

13. M.R. Stoudt, M.E. Williams, L.E. Levine, A. Creuziger, S.A. Young, J.C. Heigel, B.M. Lane and T.Q. Phan, Location-Specific Microstructure Characterization Within IN625 Additive Manufacturing Benchmark Test Artifacts, *Integr. Mater. Manuf. Innov.*, 2020, **9**, p 54–69

14. L. Levine, B. Lane, J. Heigel, K. Migler, M. Stoudt, T. Phan, R. Ricker, M. Strantza, M. Hill, F. Zhang, J. Seppala, E. Garboczi, E. Bain, D. Cole, A. Allen, J. Fox and C. Campbell, Outcomes and Conclusions from the 2018 AM-Bench Measurements, Challenge Problems, Modeling Submissions, and Conference, *Integr. Mater. Manuf. Innov.*, 2018, **9**(2020), p 1–15

15. T.Q. Phan, M. Strantza, M.R. Hill, T.H. Gnaupel-Herold, J. Heigel, C.R. D'Elia, A.T. DeWald, B. Clausen, D.C. Pagan, J.Y. Peter Ko, D.W. Brown and L.E. Levine, Elastic Residual Strain and Stress Measurements and Corresponding Part Deflections of 3D Additive Manufacturing Builds of IN625 AM-Bench Artifacts Using Neutron Diffraction, Synchrotron X-Ray Diffraction, and Contour Method, *Integr. Mater. Manuf. Innov.*, 2019, **8**, p 318–334

16. Y. Yang, M. Allen, T. London and V. Oancea, Residual Strain Predictions for a Powder Bed Fusion Inconel 625 Single Cantilever Part, *Integr. Mater. Manuf. Innov.*, 2019, **8**, p 294–304

17. A. Saboori, G. Piscopo, M. Lai, A. Salmi and S. Biamino, An Investigation on the Effect of Deposition Pattern on the Microstructure, Mechanical Properties and Residual Stress of 316L Produced by Directed Energy Deposition, *Mater. Sci. Eng. A.*, 2020, **780**, p 139179

18. Z.E. Tan, J.H.L. Pang, J. Kaminski and H. Pepin, Characterisation of Porosity, Density, and Microstructure of Directed Energy Deposited Stainless Steel AISI 316L, *Addit. Manuf.*, 2019, **25**, p 286–296

19. J.C. Haley, B. Zheng, U.S. Bertoli, A.D. Dupuy, J.M. Schoenung and E.J. Lavernia, Working Distance Passive Stability in Laser Directed Energy Deposition Additive Manufacturing, *Mater. Des.*, 2019, **161**, p 86–94

20. Y.M. Wang, T. Voisin, J.T. McKeown, J. Ye, N.P. Calta, Z. Li, Z. Zeng, Y. Zhang, W. Chen, T.T. Roehling, R.T. Ott, M.K. Santala, P.J. Depond, M.J. Matthews, A.V. Hamza and T. Zhu, Additively Manufactured Hierarchical Stainless Steels with High Strength and Ductility, *Nat. Mater.*, 2018, **17**, p 63–70

21. Design Guidelines for the Selection and Use of Stainless Steels—A Designers' Handbook Series, Nickel Institute, 2020

22. P.S. Korinko and S.H. Malene, Considerations for the Weldability of Types 304L and 316L Stainless Steel, *J. Fail. Anal. Prev.*, 2001, **1**, p 61–68

23. N. Haghdadi, M. Laleh, M. Moyle and S. Primig, Additive Manufacturing of Steels: A Review of Achievements and Challenges, *J. Mater. Sci.*, 2021, **56**, p 64–107

24. T. DebRoy, H.L. Wei, J.S. Zuback, T. Mukherjee, J.W. Elmer, J.O. Milewski, A.M. Beese, A. Wilson-Heid, A. De and W. Zhang, Additive Manufacturing of Metallic Components: Process, Structure and Properties, *Prog. Mater. Sci.*, 2018, **92**, p 112–224

25. C.A. Schneider, W.S. Rasband and K.W. Eliceiri, NIH Image to ImageJ: 25 Years of Image Analysis, *Nat. Methods.*, 2012, **9**, p 671–675

26. F. Bachmann, R. Hielscher and H. Schaeben, Texture Analysis with MTEX-Free and Open Source Software Toolbox, *Solid State Phenom.*, 2010, **160**, p 63–68

27. R. Hielscher, C.B. Silbermann, E. Schmidla and J. Ihlemannb, Denoising of Crystal Orientation Maps, *J. Appl. Crystallogr.*, 2019, **52**, p 984–996

28. W. Pantleon, Resolving the Geometrically Necessary Dislocation Content by Conventional Electron Backscattering Diffraction, *Scr. Mater.*, 2008, **58**, p 994–997

29. ASTM Standard E112-13, 2013, Standard test methods for determining average grain size, ASTM Int. (2013)

30. S. Katayama, A. Matsunawa, Solidification microstructure of laser welded stainless steels, in: ICALEO, 1984: pp. 60–67

31. A.V. Gusarov and E.P. Kovalev, Model of Thermal Conductivity in Powder Beds, *Phys. Rev. B Condens. Matter Mater. Phys.*, 2009, **80**, p 16–20

32. K.C. Mills, *Recommended Values of Thermophysical Properties for Selected Commercial Alloys*, Woodhead, Cambridge, 2004

33. U. Scipioni Bertoli, G. Guss, S. Wu, M.J. Matthews and J.M. Schoenung, In-Situ Characterization of Laser-Powder Interaction and Cooling Rates Through High-Speed Imaging of Powder Bed Fusion Additive Manufacturing, *Mater. Des.*, 2017, **135**, p 385–396

34. T. Mukherjee, H.L. Wei, A. De and T. DebRoy, Heat and Fluid Flow in Additive Manufacturing—Part II: Powder Bed Fusion of Stainless Steel, and Titanium, Nickel and Aluminum Base Alloys, *Comput. Mater. Sci.*, 2018, **150**, p 369–380

35. U. ScipioniBertoli, B.E. MacDonald and J.M. Schoenung, Stability of Cellular Microstructure in Laser Powder Bed Fusion of 316L Stainless Steel, *Mater. Sci. Eng. A.*, 2019, **739**, p 109–117

36. K. Saeidi, X. Gao, Y. Zhong and Z.J. Shen, Hardened Austenite Steel with Columnar Sub-grain Structure Formed by Laser Melting, *Mater. Sci. Eng. A.*, 2015, **625**, p 221–229

37. V.D. Manvatkar, A.A. Gokhale, G. JaganReddy, A. Venkataramana and A. De, Estimation of Melt Pool Dimensions, Thermal Cycle, and Hardness Distribution in the Laser-Engineered Net Shaping Process of Austenitic Stainless Steel, *Metall. Mater. Trans. A Phys. Metall. Mater. Sci.*, 2011, **42**, p 4080–4087

38. N. Suutala, T. Takalo and T. Moisio, Ferritic-Austenitic Solidification Mode in Austenitic Stainless Steel Welds, *Metall. Trans. A.*, 1980, **11**, p 717–725

39. J.A. Brooks and A.W. Thompson, Microstructural Development and Solidification Cracking Susceptibility of Austenitic Stainless Steel Welds, *Int. Mater. Rev.*, 1991, **36**, p 16–44

40. J.C. Lippold and W.F. Savage, Solidification of Austenitic Stainless Steel Weldments—2. The Effect of Alloy Composition on Ferrite Morphology, *Weld. J.*, 1980, **59**, p 48

41. M.J. Cieslak and W.F. Savage, Weldability and Solidification Phenomena of Cast Stainless Steel, *Weld. J.*, 1980, **59**, p 136–146

42. Y. Strausser, 30. X-Ray Diffraction (XRD), in: Charact. Silicon Process., Elsevier, 1993

43. A.L. Schaeffler, Constitution Diagram for Stainless Steel Weld Metal, *Met. Prog.*, 1949, **56**, p 680-680B

44. D. Séférian, *Métallurgie de La Soudure*, Dunod, Paris, 1959

45. J.C. Lippold and D.J. Kotecki, *Welding Metallurgy and Weldability of Stainless Steels*, Wiley, New York, 2005

46. S.A. David, J.M. Vitek, R.W. Reed, T.L. Hebble, Effect of Rapid Solidification on Stainless Steel Weld Metal Microstructures and Its Implications on the Schaeffler Diagram, United States, 1987

47. M. Letenneur, A. Kreitcberg and V. Brailovski, The Average Grain Size and Grain Aspect Ratio in Metal Laser Powder Bed Fusion: Modeling and Experiment, *J. Manuf. Mater. Process.*, 2020, **4**, p 25

48. N.J. Petch, The Cleavage Strength of Crystals, *J. Iron Steel Inst.*, 1953, **174**, p 25

49. E.O. Hall, The Deformation and Ageing of Mild Steel: III Discussion of Results, *Proc. Phys. Soc. Sect. B.*, 1951, **64**, p 747–753

50. M.S. Pham, B. Dovgyy, P.A. Hooper, C.M. Gourlay and A. Piglione, The Role of Side-Branching in Microstructure Development in Laser Powder-Bed Fusion, *Nat. Commun.*, 2020, **11**, p 1–12

51. J.J. Marattukalam, D. Karlsson, V. Pacheco, P. Beran, U. Wiklund, U. Jansson, B. Hjörvarsson and M. Sahlberg, The Effect of Laser Scanning Strategies on Texture, Mechanical Properties, and Site-Specific Grain Orientation in Selective Laser Melted 316L SS, *Mater. Des.*, 2020, **193**, p 108852

52. Y. Kok, X.P. Tan, P. Wang, M.L.S. Nai, N.H. Loh, E. Liu and S.B. Tor, Anisotropy and Heterogeneity of Microstructure and Mechanical Properties in Metal Additive Manufacturing: A Critical Review, *Mater. Des.*, 2018, **139**, p 565–586

53. A. Yadollahi and N. Shamsaei, Additive Manufacturing of Fatigue Resistant Materials: Challenges and Opportunities, *Int. J. Fatigue.*, 2017, **98**, p 14–31

54. A. Riemer, S. Leuders, M. Thöne, H.A. Richard, T. Tröster and T. Niendorf, On the Fatigue Crack Growth Behavior in 316L Stainless Steel Manufactured by Selective Laser Melting, *Eng. Fract. Mech.*, 2014, **120**, p 15–25

55. T.S. Huang and G.S. Frankel, Influence of Grain Structure on Anisotropic Localised Corrosion Kinetics of AA7XXX-T6 Alloys, *Corros. Eng. Sci. Technol.*, 2006, **41**, p 192–199

56. K.A. Small, Z. Clayburn, R. DeMott, S. Primig, D. Fullwood and M.L. Taheri, Interplay of Dislocation Substructure and Elastic Strain Evolution in Additively Manufactured Inconel 625, *Mater. Sci. Eng. A.*, 2020, **785**, p 139380

57. T. Skippon, L. Balogh and M.R. Daymond, Comparison of Electron Backscatter and X-Ray Diffraction Techniques for Measuring Dislocation Density in Zircaloy-2, *J. Appl. Crystallogr.*, 2019, **52**, p 415–427